Article

Ni-BaMnO$_3$ Perovskite Catalysts for NO$_x$-Assisted Soot Oxidation: Analyzing the Effect of the Nickel Addition Method

Salvador Montilla-Verdú, Álvaro Díaz-Verde [ID], Verónica Torregrosa-Rivero [ID] and María José Illán-Gómez *[ID]

MCMA Group, Department of Inorganic Chemistry and Materials Institute (IUMA), Faculty of Sciences, University of Alicante, Ap. 99, E-03080 Alicante, Spain; salvador.montilla@ua.es (S.M.-V.); alvaro.diaz@ua.es (Á.D.-V.); vero.torregrosa@ua.es (V.T.-R.)
* Correspondence: illan@ua.es

Abstract: In this study, we analyzed the role of a series of BaMn$_{1-x}$Ni$_x$O$_3$ (x = 0, 0.2, and 0.4) mixed oxide catalysts, synthesized using the sol–gel method, in NO$_x$-assisted diesel soot oxidation. ICP-OES, XRD, XPS, and H$_2$-TPR techniques were used for characterization and Temperature-Programmed Reaction experiments (NO$_x$-TPR and Soot-NO$_x$-TPR), and isothermal reactions at 450 °C (for the most active sample) were carried out to determine the catalytic activity. All samples catalyzed NO and soot oxidation at temperatures below 400 °C, presenting nickel-containing catalysts with the highest soot conversion and selectivity to CO$_2$. However, the nickel content did not significantly modify the catalytic performance, and in order to improve it, two catalysts (5 wt % in Ni) were synthesized via the hydrothermal method (BMN2H) and the impregnation of nickel on a BaMnO$_3$ perovskite as support (M5). The two samples presented higher activity for NO and soot oxidation than BMN2E (obtained via the sol–gel method) as they presented more nickel on the surface (as determined via XPS). BMN2H was more active than M5 as it presented (i) more surface oxygen vacancies, which are active sites for oxidation reactions; (ii) improved redox properties; and (iii) a lower average crystal size for nickel (as NiO). As a consequence of these properties, BMN2H featured a high soot oxidation rate at 450 °C, which hindered the accumulation of soot during the reaction and, thus, the deactivation of the catalyst.

Keywords: perovskite; nickel; manganese; NO$_X$; soot oxidation; diesel

1. Introduction

It is well known that car engines are one of the main sources of atmospheric pollution. For this reason, electric and fuel-cell-based engines have been proposed as alternatives to internal combustion engines (ICEs). However, these new engines present drawbacks that make them less viable than ICEs [1,2]. Therefore, it is expected that ICEs, such as diesel and gasoline engines, will remain the leader of primary power generation in the automotive sector. Diesel engines present higher efficiency and durability than gasoline engines [3,4]; however, the former generates soot particles and nitrogen oxides (NO$_X$), presenting notably dangerous effects for both humans and the environment. Soot particles can affect the respiratory tract, causing cardiovascular problems, while NO$_X$ is responsible for photochemical smog and acid rain [5–8]. Because of this, strict limits have been established through European legislation for the protection of environmental and human health [9,10]. To accomplish this regulation for automotive diesel engines, a diesel oxidation catalyst (DOC), followed by a diesel particulate filter (DPF), has been proposed as an effective after-treatment system. In this sense, commercially available devices are composed of a ceramic monolith coated with noble metals (Pt, Pt/Pd, or Pd/Rh) that are scarce and expensive [11–13].

Perovskite-type mixed oxides (ABO_3) are widely used in industry due to their low price, high stability, and good optical, magnetic, electronic, and ferroelectric properties [14]. Additionally, perovskites present interesting catalytic properties that mainly depend on the nature of B metal and that can be modulated by adding some transition metals able to improve their redox properties (associated with the oxidation state of B metal and the formation of oxygen vacancies) and, therefore, catalytic activity [15,16]. Recent results have revealed that these catalysts can be used for the control of pollutants generated by ICEs [17,18]. Accordingly, perovskites could be used for soot removal from diesel engines [19–23].

In a previous study [23], a series of $BaFe_{1-x}Ni_xO_3$ (x = 0, 0.2, 0.4, and 0.8) catalysts were used to catalyze NO_x-assisted diesel soot oxidation, allowing for determining the effect of the partial substitution of Fe by Ni. $BaFeO_3$ and $BaFe_{0.6}Ni_{0.4}O_3$ are the best catalysts, but the latter is more stable as it contains the highest proportion of Ni(II) on the surface, featuring the highest initial soot oxidation rate and the lowest amount of unreacted soot after the reaction. Thus, in this study, Mn was partially substituted by Ni in $BaMnO_3$ perovskite to evaluate if the presence of Ni could improve the catalytic activity of $BaMnO_3$ perovskite in NO_x-assisted diesel soot oxidation [21]. To achieve this purpose, a series of $BaMn_{1-x}Ni_xO_3$ (x = 0, 0.2, and 0.4) samples were synthesized (using the sol–gel method), deeply characterized (via ICP-OES, XRD, XPS, and H_2-TPR), and tested as catalysts in NO to NO_2 oxidation and NO_x-assisted diesel soot oxidation. Temperature-Programmed Reaction experiments (NO_x–TPR and Soot–NO_x–TPR) and, for the best catalyst, isothermal reactions at 450 °C were developed. Additionally, as the nickel content did not significantly modify the catalytic performance, two additional nickel catalysts (5 wt %) were obtained using the hydrothermal method (BMN2H) and wetness impregnation of nickel on a $BaMnO_3$ perovskite support (M5).

2. Results and Discussion

2.1. BaMn_{1−x}Ni_xO_3 Catalysts: Effect of Nickel Content

2.1.1. Chemical and Morphological Properties

Table 1 shows the nomenclature, the actual nickel content (wt %) obtained via ICP–OES, the nominal nickel content (wt %) calculated from the catalyst formula, and the BET surface area, as well as various XRD data.

**Table 1.** Nickel content, BET surface area, and XRD data.

Sample	Nomenclature	BET Surface Area (m^2/g)	Nominal Ni (wt %)	Actual Ni (wt %)	2θ for Main Peak of $BaMnO_3$ (°)	NiO Average Crystal Size (nm)
$BaMnO_3$	BME	7	-	-	31.4	-
$BaMn_{0.8}Ni_{0.2}O_3$	BMN2E	5	4.8	4.8	31.4	30
$BaMn_{0.6}Ni_{0.4}O_3$	BMN4E	6	9.6	9.5	31.4	35

From a general point of view, the actual Ni content is very close to the nominal one, indicating that the method used for synthesis achieves the required amount of this metal. Moreover, the samples present a low BET surface area, as corresponds to mixed oxides with very low porosity development, such as perovskites [15,19–25].

2.1.2. Crystalline Structure

XRD patterns for $BaMn_{1-x}Ni_xO_3$ samples are featured in Figure 1. The hexagonal $BaMnO_3$ perovskite-type structure is detected for the BME sample, but for the two samples with nickel, this structure coexists with the stoichiometric $BaNiO_3$ hexagonal structure and with an oxygen-deficient hexagonal perovskite structure $BaNiO_{2.55}$. Thus, it seems that nickel is not inserted into the $BaMnO_3$ perovskite structure and, instead of that, it forms two Ni-based perovskites. This fact, which was previously found for $BaFe_{1-x}Ni_xO_3$ catalyst

series [20–23], seems to be justified by the values of the tolerance factor (*t*), calculated using the ionic radius of the components of perovskites (Ba^{2+}: 175 pm, Mn^{3+}: 65 pm, Ni^{2+}: 78 pm, and O^{2-}: 140 pm, corresponding to coordination numbers 12, 6, and 6 for cation A, cation B, and oxygen, respectively) [26] and shown in Table 2. So, as the *t* value is closer to 1 (theorical value) for BaNiO$_3$ than for BaMn$_{1-x}$Ni$_x$O$_3$ perovskites, Ni is not inserted into the BaMnO$_3$ perovskite structure. Instead of that, it forms the BaNiO$_3$ and BaNiO$_{2.55}$ perovskites. Note that for Ni samples, the location (2θ value) of the main diffraction peak of the hexagonal perovskite structure is not modified in the presence of Ni (Table 1), which corroborates that this metal has not been inserted into the perovskite framework [20–23] as it was previously detected for BaMn$_{1-x}$Cu$_x$O$_3$ samples [21,25].
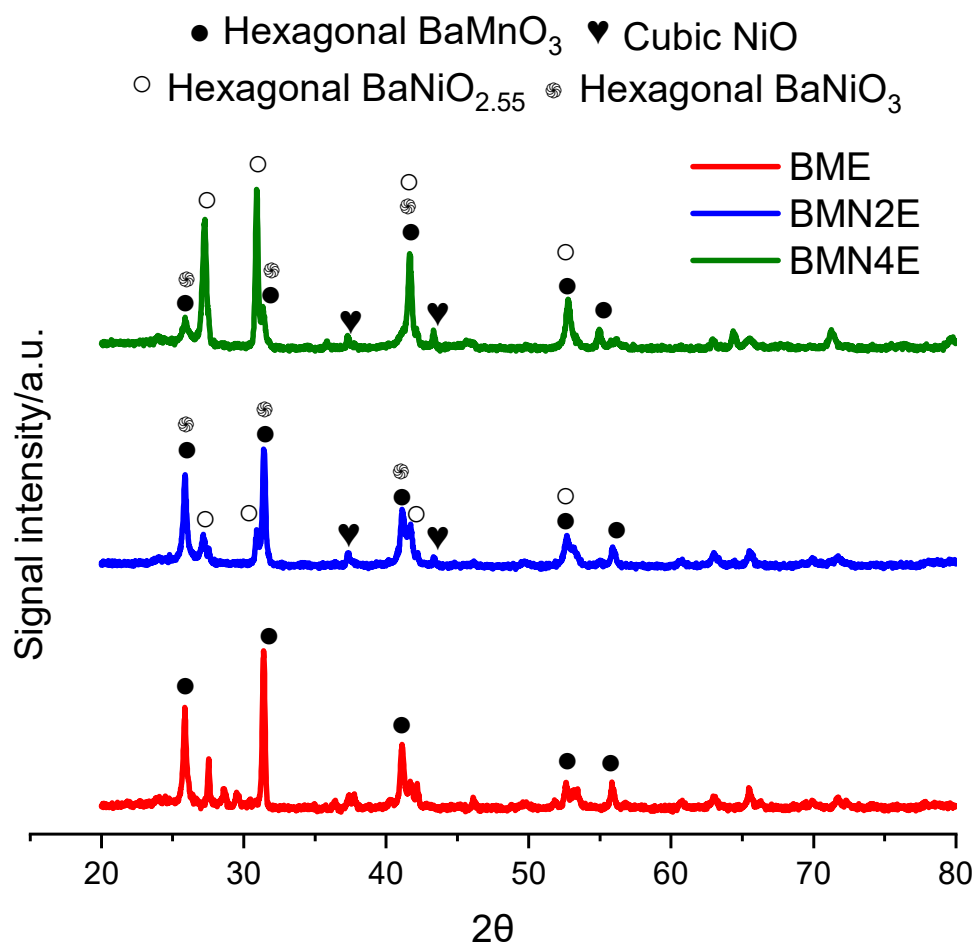
Figure 1. XRD patterns for BaMn$_{1-x}$Ni$_x$O$_3$ samples.

Table 2. Tolerance factor values.

Sample	*t* Factor (Ni^{2+}, Fe^{3+})
BaMnO$_3$	1.09
BaMn$_{0.8}$Ni$_{0.2}$O$_3$	1.07
BaMn$_{0.6}$Ni$_{0.4}$O$_3$	1.06
BaNiO$_3$	1.02

Additionally, in the XRD patterns of the BMN2E and BMN4E samples, peaks corresponding to NiO, whose intensity increases with nickel content, are detected. By using the Scherrer equation, the average crystal size of NiO for the BMN2E and BMN4E samples was calculated (Table 1), increasing with the nickel percentage.

2.1.3. Surface Properties

The XPS spectra for the Ni $2p^{3/2}$ (Figure 2a), Mn $2p^{3/2}$ (Figure 2b), and O 1s (Figure 2c) transitions for BaMn$_{1-x}$Ni$_x$O$_3$ samples are illustrated in Figure 2.
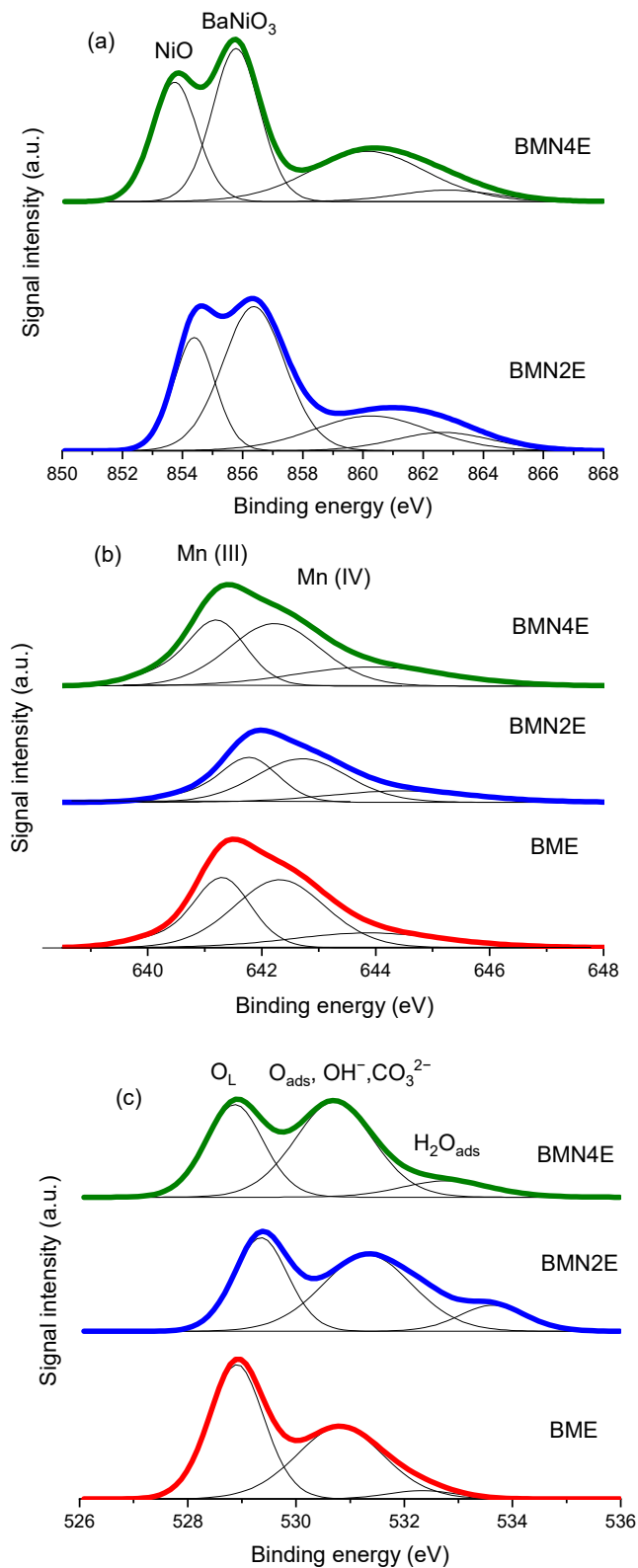
Figure 2. XPS spectra of the (**a**) Ni $2p^{3/2}$, (**b**) Mn $2p^{3/2}$, and (**c**) O1s transitions for BaMn$_{1-X}$Ni$_X$O$_3$ samples.

Focusing the attention on Figure 2a, according to the literature [27–30], binding energy (BE) values between 854 and 856 eV reveal the presence of Ni(II), Ni(III), and Ni (IV) species on the surface, with the existence of Ni(II) supported by the satellite peaks at 860 and 864 eV. So, as it is common on perovskites [26,28–30], high oxidation states for Ni (Ni(III) and Ni(IV)) seem to be present on the surface to compensate for the oxidation states of B metal found in BMN2E and BMN4E perovskites. After the deconvolution of the main signal, two components are found, corresponding to (i) Ni from $BaNiO_3$ perovskite (which could be Ni(II), Ni(III), and Ni(IV)) at higher binding energies, and (ii) Ni from NiO at lower binding energies [23].

Table 3 shows the XPS nickel percentage and the percentage of total nickel (determined by ICP–OES), the proportion of surface nickel (calculated as $100 \times$ [Ni(%) XPS/Ni(%) ICP–OES]), and the $NiO/BaNiO_3$ surface ratio (obtained from the area of the deconvoluted peaks assigned to Ni as NiO and Ni as $BaNiO_3$). For the BMN2E and BMN4E samples, the percentage of surface nickel is lower than 100% and, consequently, all of nickel added is not located on the surface. However, the percentage of surface nickel (surface Ni (%)) and the proportion of Ni which is as NiO (indicated by $NiO/BaNiO_3$ ratio) increases with the Ni percentage, suggesting that the formation of $BaNiO_3$ is being disfavored with respect to NiO.

Table 3. XPS data of $BaMn_{1-X}Ni_XO_3$ samples.

Samples	B.E Max Mn(III) (eV)	B.E Max Mn(VI) (eV)	B.E Max O_L (eV)	Ni (wt %) ICP-OES	Ni (wt %) XPS	Surface Ni (%) [1]	NiO/ $BaNiO_3$ [2]	Mn(IV)/ Mn(III)	O_L/ Mn+Ni+Ba
BME	641.3	642.4	528.9	-	-	-	-	1.4	0.9
BMN2E	641.8	642.8	529.4	4.8	3.5	73	0.5	1.4	0.8
BMN4E	641.2	642.2	529.0	9.5	8.0	84	0.7	1.3	0.7

[1] Calculated as $100 \times$ [Ni (%) XPS/Ni(%) ICP-OES], [2] Obtained from the area of the deconvoluted peaks assigned to Ni as NiO and as $BaNiO_3$.

Figure 2b presents the deconvolution for the Mn $2p^{3/2}$ transition. The band between 641 and 642 eV corresponds to Mn(III) (this assignation is supported by the satellite peak located at 645 eV, and the band detected between 642 and 644 eV reveals that Mn(IV) is also present [19,21,22,25,31]). Table 3 displays the Mn(IV)/Mn(III) surface ratios (estimated considering the area of the corresponding deconvoluted peaks). According to the perovskite stoichiometry ($BaMnO_3$), Mn should be as Mn(IV) for the neutrality of positive and negative charges. However, as Mn(III) and Mn(IV) coexist on the surface, oxygen vacancies have to be present on the surface. The existence of Mn(III) on the surface also seems to justify that Ni(II) is being oxidized to Ni(III)/Ni(IV). Note that as the Mn(IV)/Mn(III) ratio is higher than one for the three samples (without a clear trend with nickel content), Mn(IV) seems to be the main oxidation state. It is well known that manganese-based perovskites, due to their redox properties related to the electronic configuration of Mn(III) and Mn(IV) [32–34], are active catalysts for oxidation reactions, and the coexistence of the two oxidation states, but specially an enriched surface of Mn(IV), increases the oxygen mobility and, consequently, the catalytic activity [35]. Finally, it is observed that the maximum of the BE corresponding to the Mn(IV) and Mn(III) deconvoluted signals is different for nickel-containing samples due to the presence of nickel species on surface.

Figure 2c exhibits the spectra for the O 1s transition for $BaMn_{1-x}Ni_xO_3$ samples. According to literature [31–37], the O 1s spectrum for perovskites is usually deconvoluted into three bands: (i) the band at around 530 eV corresponds to lattice oxygen (O_L), (ii) the band at around 531 eV is associated with surface oxygen species such as adsorbed oxygen, hydroxyl, and carbonate groups, and finally, (iii) the band related to adsorbed water appears at 533 eV. The three bands are detected for all samples, with O_L being the main one. In Table 3, the $O_L/(Ba_L+Mn+Ni)$ ratio (estimated from the areas of the O_L deconvoluted band and of the bands corresponding to cations) is included, as well as the BE of the maximum of this deconvoluted band. As all $O_L/(Ba_L+Mn+Ni)$ ratios are lower than the nominal one

(1.5), oxygen vacancies exist on the surface, and as the values are lower for nickel containing samples, more oxygen vacancies are present in these two samples. Additionally, a shift towards higher values of the BE maximum for the O_L deconvoluted band is observed due to the presence of nickel on the surface.

2.1.4. Reducibility

The reducibility of $BaMn_{1-X}Ni_XO_3$ samples was determined by a Temperature-Programmed Reduction with H_2 (H_2–TPR), with the profiles shown in Figure 3, in which several reduction peaks between 200 °C and 1000 °C, corresponding to the reduction of Mn and Ni/Mn, were detected.
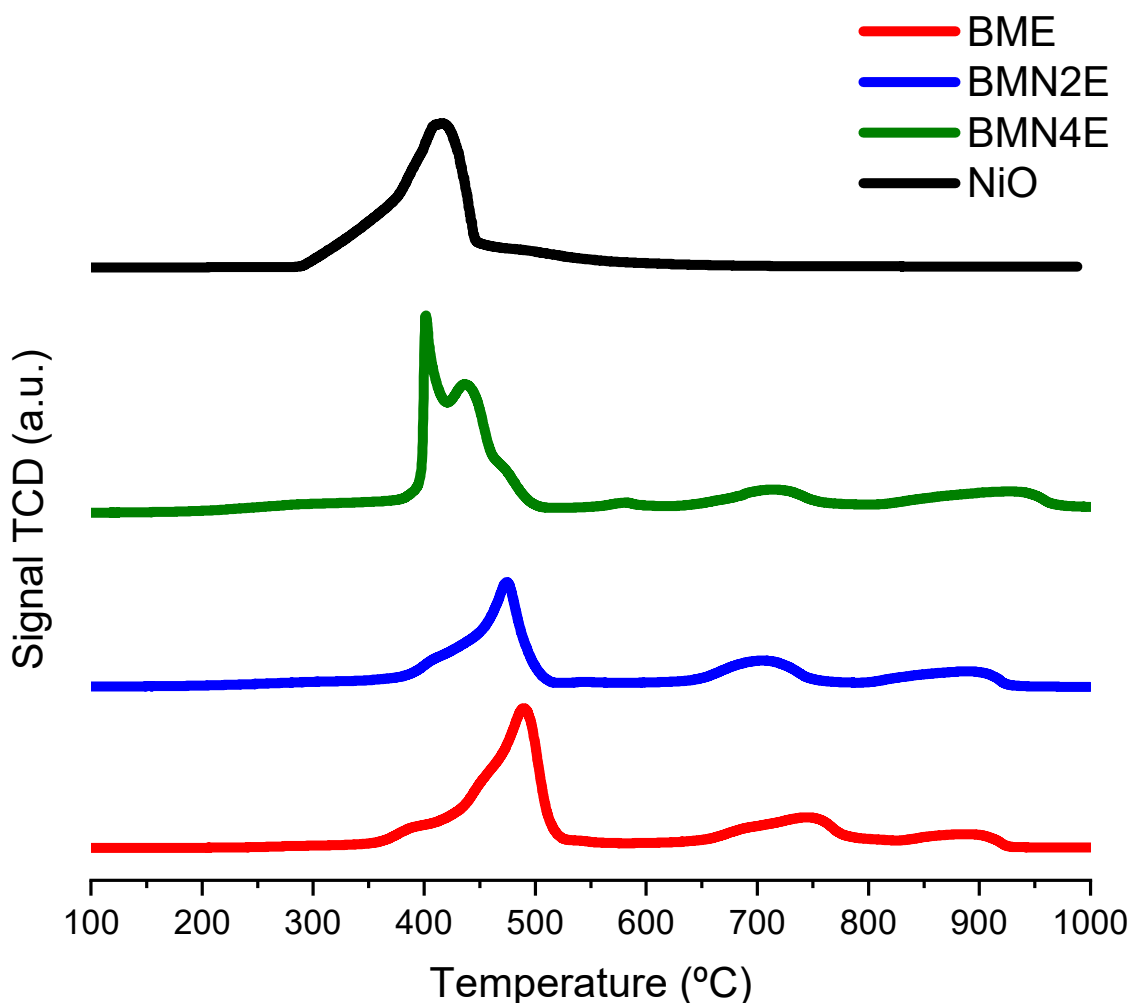
Figure 3. H_2–TPR profiles for $BaMn_{1-x}Ni_xO_3$ samples.

The H_2–TPR profile of BME presents three reduction peaks [19,21,22,25,38]: (i) the first peak at temperatures between 400 °C and 500 °C corresponds to the reduction of Mn(IV) and Mn(III) to Mn(II), (ii) the peak at intermediate temperatures, from 700 °C to 800 °C, is due to the desorption of surface oxygen species, and finally, (iii) the peak at high temperatures (850–1000 °C) is assigned to the reduction of Mn(II) to Mn(0). BMN2E features the same three reduction peaks that were detected for BME, but the peak at the lowest temperature includes the reduction of Mn(IV)/Mn(III) to Mn(II) and, also, the reduction of Ni(II) to Ni(0) [23,39], according to the reduction profile of the NiO used as reference for nickel reduction. For BMN2E and BMN4E, all the reduction peaks are located at lower temperatures than for BME, so as it was previously observed for the $BaMn_{1-x}Cu_xO_3$ samples [21,25,40], the incorporation of Ni favors the reduction of manganese, revealing a

Mn–Ni synergistic effect. For BMN4E, the low temperature reduction peak is more complex and shows two well-defined maxima that should correspond to two reduction processes. Furthermore, as the signal intensity does not decrease in the intermediate area between both maxima, the presence of a third overlapping peak is suggested. Thus, a tentative assignment of these peaks could be [23,40]: (i) the peak with the maximum at about 390 °C corresponds to the reduction of Ni(II) with a low interaction with the support and, thus, the reduction of NiO species, (ii) the overlapped peak at intermediate temperatures, about 430 °C, is assigned to the reduction to Ni(0) of the NiO_x species on the surface and subsurface of the support, and of Ni(II) with a stronger interaction with the perovskite, and finally, (iii) the peak with a defined maximum at 460 °C corresponds to the reduction of Mn(IV) and Mn(III) to Mn(II).

Thus, based on H_2–TPR profiles, the BMN2E catalyst seems to have more nickel with a stronger interaction with the $BaMnO_3$ support, which improves the Ni–Mn synergistic effect and, consequently, the temperature for the manganese reduction is decreased. On the other hand, the BMN4E catalyst seems to present a higher proportion of nickel with a low interaction with the perovskite and, therefore, is reducible at lower temperature (390 °C). This peak appears clearly differentiated in this catalyst due to the higher amount of NiO species. Finally, the asymmetry of the main reduction peak of BMN2E at low temperatures reveals the presence of a low amount of NiO, as also observed via XRD and XPS.

2.1.5. Catalytic Activity Tests

NO to NO_2 Oxidation (NO_x–TPR)

The catalytic activity for the NO oxidation was determined by Temperature-Programmed Reaction (NO_x–TPR) experiments.
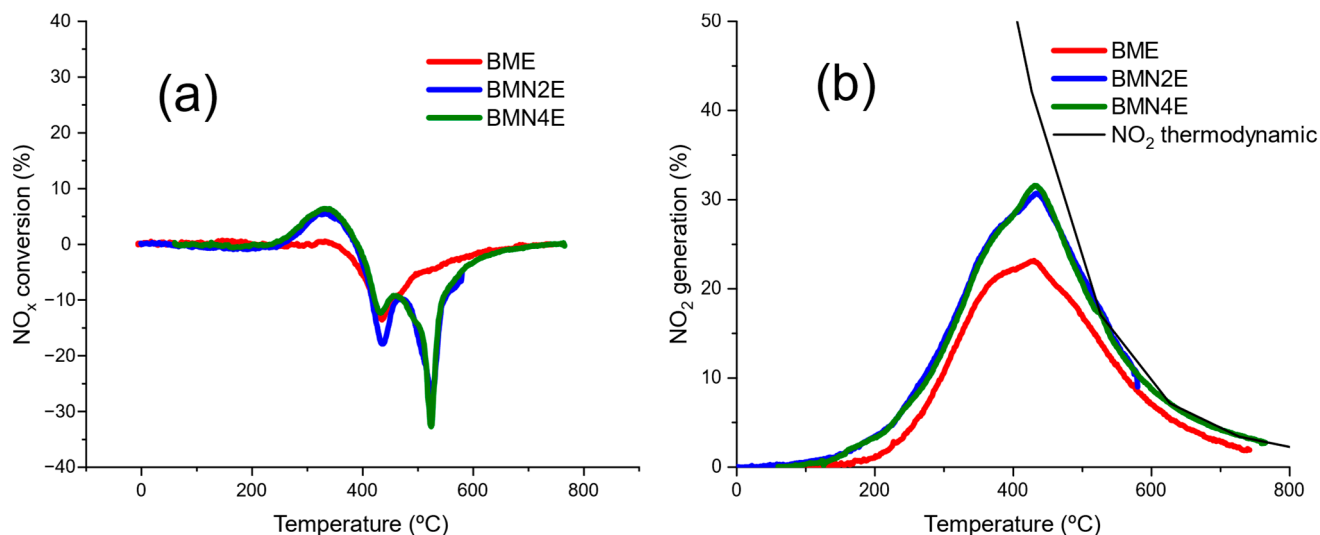
Figure 4a shows the NO_X conversion profiles as a function of temperature for the three samples. Considering Equation (1), a positive value of NO_x conversion indicates that the adsorption of NO_x on the sample is taking place as the amount of NO_x detected at the outlet of the reactor (so, after reaction) is lower than the measured at the inlet of the reactor (so, before reaction). On the other hand, a negative means that NO_x desorption occurs. Note that the amount of desorbed NO_x is higher than the amount of adsorbed NO_X because the adsorption of NO_X at room temperature taking place before the test starts is not registered. BME does not present a significant adsorption capacity, but nickel-containing catalysts (BMN2E and BMN4E) show some adsorption ability. In fact, for these catalysts, two different desorption peaks are observed: (i) a peak with a minimum at about 420 °C, which is at the same temperature as the minimum shown by the raw perovskite BME and, therefore, could be associated with the desorption of NO_x adsorbed at room temperature on the perovskite; and (ii) an intense peak with a minimum at around 520 °C which is not detected for the raw perovskite and has to be related to the presence of nickel species, which would be able to adsorb NO_x. Note that the intensity of this peak increases with respect to the peak at lower temperatures as the nickel content increases.

Figure 4b presents the NO_2 generation profiles during NO_x–TPR experiments. First of all, it must be underlined that the real value of NO_2 generated cannot be obtained from these profiles because, as indicated in Figure 4a, a fraction of this NO_2 is being adsorbed on the catalyst surface so it is not detected [23]. Thus, these profiles show only the NO_2 evolved. Note that all catalysts are active for the oxidation of NO to NO_2 at temperatures below ca 400 °C, where the oxidation capacity is higher for the two nickel samples, so nickel should present at active sites for the NO oxidation [23]. However, the NO_2 that evolves is similar for BMN2E and BMN4E, featuring a maximum of around 32% at 430 °C.

Soot Oxidation (Soot–NO_x–TPR)

Figure 5a shows the soot conversion profiles of $BaMn_{1-x}Ni_xO_3$ catalysts. At temperatures below 600 °C [21,22], which is the range of temperature relevant for soot removal from diesel engines, all catalysts present conversion values higher than the observed for uncatalyzed reactions (blank in Figure 5a). BMN2E and BMN4E are the most active catalysts for

soot removal, and they also evolve a higher amount of NO_2 than the raw perovskite (BME) (see Figure 4b). This is because NO_2 is more effective than O_2 for soot oxidation [19–23], so the catalysts evolving a higher percentage of NO_2 should also be the catalysts showing higher soot conversion percentage. Thus, if Figure 5b is compared with Figure 4b (corresponding to the NO_2 evolved in the presence and in the absence of soot), it is concluded that around 65% of the NO_2 evolved is used for soot oxidation.

Figure 4. (**a**) NO_X conversion and (**b**) NO_2 generation profiles in TPR conditions for $BaMn_{1-x}Ni_xO_3$ samples.
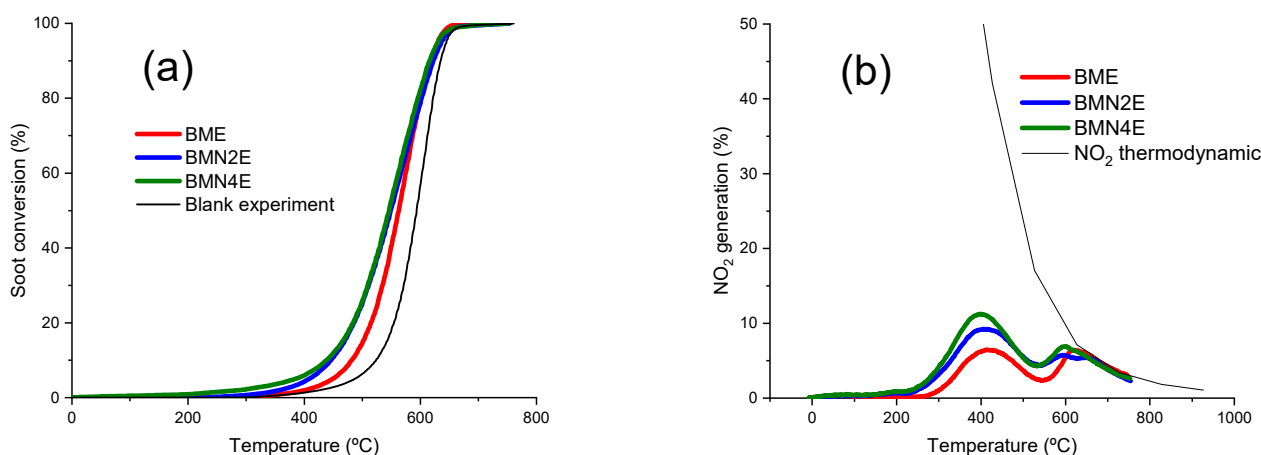
Figure 5. (**a**) Soot conversion and (**b**) NO_2 generation profiles in TPR conditions for $BaMn_{1-x}Ni_xO_3$ samples.

From these conversion profiles, the temperature to achieve 50% soot conversion ($T_{50\%}$) was determined and is included in Table 4, where the selectivity to CO_2 (calculated by Equation (4)) is also featured. As expected, a higher selectivity to CO_2 and a lower $T_{50\%}$ value is found for all samples than for uncatalyzed reactions (blank in figure) [21–23,41]. BMN2E and BMN4E present a lower $T_{50\%}$ value and a higher selectivity to CO_2 than BME as nickel samples present additional active sites for soot oxidation.

In conclusion, nickel samples are more active for the oxidation of NO to NO_2 and, consequently, for soot r oxidation than BME, but the nickel content is not relevant. Thus, the different properties of BMN2E and BMN4E seem to not significantly affect the performance for soot oxidation. Note that BMN4E presents a higher percentage of surface Ni, a higher amount of surface oxygen vacancies, and a higher reducibility than BMN2E, but it also presents a larger average crystal size. Thus, although BMN2E shows a lower percentage of surface nickel, the average crystal size is lower than for BMN4E, so the amount of nickel

active sites should be similar, with both samples presenting almost the same catalytic activity. For this reason, BMN2E, with the lowest nickel percentage (5 wt %), has been selected to analyze the effect of the nickel addition method in the next section.

Table 4. $T_{50\%}$ and selectivity to CO_2 for $BaMn_{1-x}Ni_xO_3$ samples.

Sample	$T_{50\%}$ (°C)	Selectivity to CO_2 (%)
BME	563 ± 8	75
BMN2E	548 ± 8	84
BMN4E	546 ± 8	83
Blank	593 ± 8	38

2.2. Effect of Nickel Addition Method

To analyze the effect of the nickel addition method, two samples with 5 wt % nickel were prepared by hydrothermal synthesis (denoted as BMN2H) and by incipient wetness impregnation (designed as M5) using BME as a support. In the following sections, the characterization results will be presented and discussed as well as their catalytic performance, which will be compared with the one shown by the sample prepared via the sol–gel method (BMN2E) discussed in the previous section.

2.2.1. Characterization of BMN2H and M5 Catalysts

As well as for the BMN2E sample, the BET surface areas of BMN2H and M5 (5 and 6 m^2/g, respectively) reveal that these samples present a very-low-developed porosity [15, 24]. On the other hand, their actual Ni content is similar (4.9 wt % Ni for both samples) to the nominal one (5.0 wt % Ni), so the procedure used for nickel incorporation also achieves the required amount of this metal.

XRD patterns for the two samples are shown in Figure 6. The main crystalline phase is the hexagonal perovskite-type structures. As the angle of the maximum of the $BaMnO_3$ main diffraction peak does not change (Table 5), it seems that, as for the BMN2E sample, nickel is not inserted into the $BaMnO_3$ perovskite framework [23] and it forms the $BaNiO_3$ perovskite. For BMN2H, the $BaNiO_{2.55}$ perovskite structure is also detected. However, for M5, only the stoichiometric $BaNiO_3$ perovskite structure is formed; so, it is expected that this sample presents a smaller amount of oxygen vacancies than the BMN2H sample. Additionally, the peaks corresponding to cubic NiO are detected for the two samples as a minority crystal phase. In Table 5, the average crystal size data of NiO is included and is higher for M5 than for BMN2H. Finally, BMN2H also shows peaks corresponding to a $BaCO_3$ phase, so this is the most heterogeneous sample. Thus, these results reveal that the nickel addition method is relevant as it determines not only the crystalline phases but also the NiO average crystal size and therefore the amount of nickel active sites, which should be higher for the BMN2H sample.

Table 5. XRD data.

Sample	2θ for Main Peak of $BaMnO_3$ (°)	NiO Average Crystal Size (nm)
M5	31.4	24
BMN2H	31.4	19

The Ni $2p^{3/2}$ (Figure 7a), Mn $2p^{3/2}$ (Figure 7b), and O 1s (Figure 7c) XPS spectra of the M5 and BMN2H samples are compared in Figure 7, where the Ni, Mn, and O contributions described for BMN2E (see Figure 3 and related discussion) are also detected [19,21–23,25,28–37].
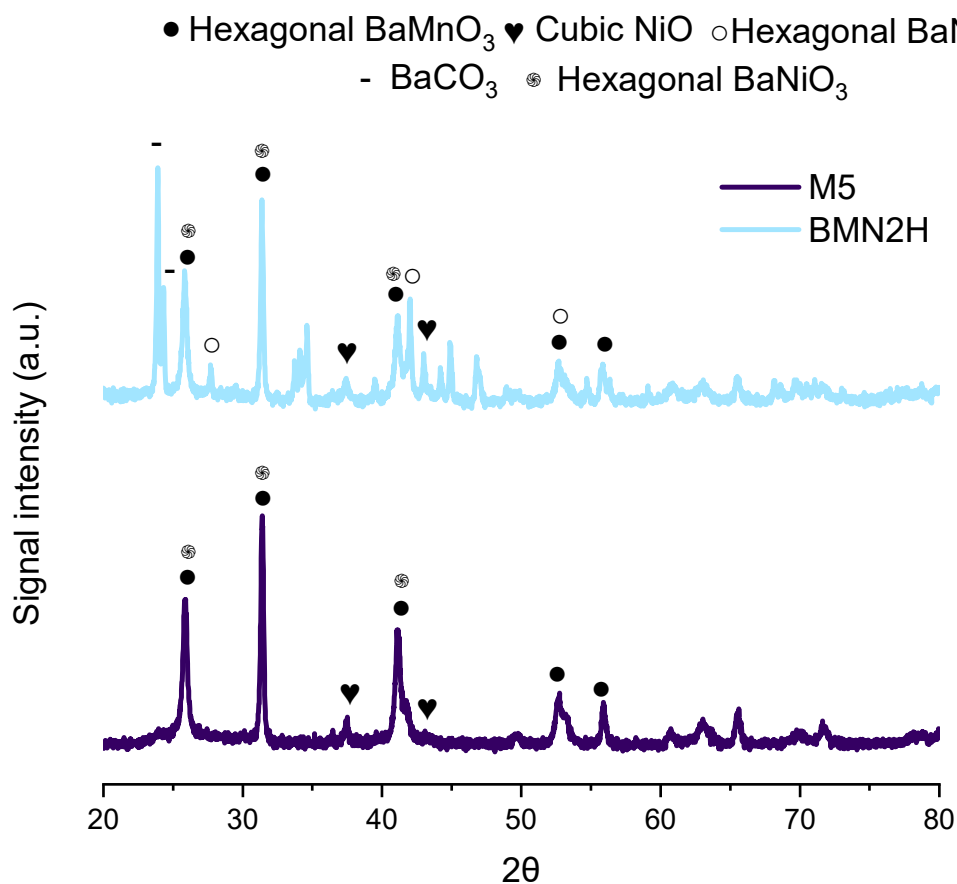
Figure 6. XRD patterns for M5 and BMN2H samples.

Table 6 compares the surface nickel percentage, calculated from XPS data, with the actual nickel percentage (determined by ICP–OES) and with the $NiO/BaNiO_3$ surface ratio (obtained from the areas of the corresponding deconvoluted peaks). M5 and BMN2H present a percentage of surface nickel much higher than the one determined by ICP–OES (the actual nickel percentage), which indicates that nickel is being accumulated on the surface. Note that M5 presents the highest content of surface nickel, which could be expected as the metal has been added by the impregnation method. So, based on the $NiO/BaNiO_3$ ratio, M5 is the sample presenting the highest proportion of NiO on the surface and it also features the highest average crystal size for NiO, as calculated from the XRD data.

Table 6. XPS characterization data for M5 and BMN2H samples.

Catalyst	B.E Max Mn(III) (eV)	B.E Max Mn(VI) (eV)	B.E Max O_L (eV)	Ni (wt %) ICP-OES	Ni (wt %) XPS	Surface Ni (%) [1]	NiO/ BaNiO$_3$ [2]	Mn(IV)/ Mn(III)	O_L/ Mn+Ni+Ba
M5	641.5	643.1	529.0	4.9	20.2	412	0.7	0.6	2.0
BMN2H	641.2	642.3	528.9	4.9	9.8	200	0.9	0.9	1.1

[1] Calculated as $100 \times$ [Ni (%) XPS/Ni(%) ICP-OES]. [2] Obtained from the area of the deconvoluted peaks assigned to Ni as NiO and as BaNiO$_3$.

Table 6 shows the Mn(IV)/Mn(III) surface ratios, estimated considering the area of the deconvoluted peaks. As Mn(IV)/Mn(III) is lower than one for M5, this sample presents a higher proportion of Mn(III) than Mn(IV) on the surface. BMN2H features an almost similar proportion of the two oxidation states as the ratio is close to one. As Mn(III) and Mn(IV) coexist on the catalyst surface, a defect of positive charge exists that will be compensated for by the formation of surface oxygen vacancies (and by the presence of Ni(III) and Ni(IV));

there will be a higher amount for the sample with a lower Mn(IV)/Mn(III) ratio, as is the case with M5. On the other hand, for BMN2H, the corresponding deconvoluted signals of Mn(III) and Mn(IV) appear at lower binding energies than for M5. Thus, as this sample also presents a higher proportion of Mn(IV) on the surface, it is expected that BMN2H features a better redox behavior than the M5 sample.
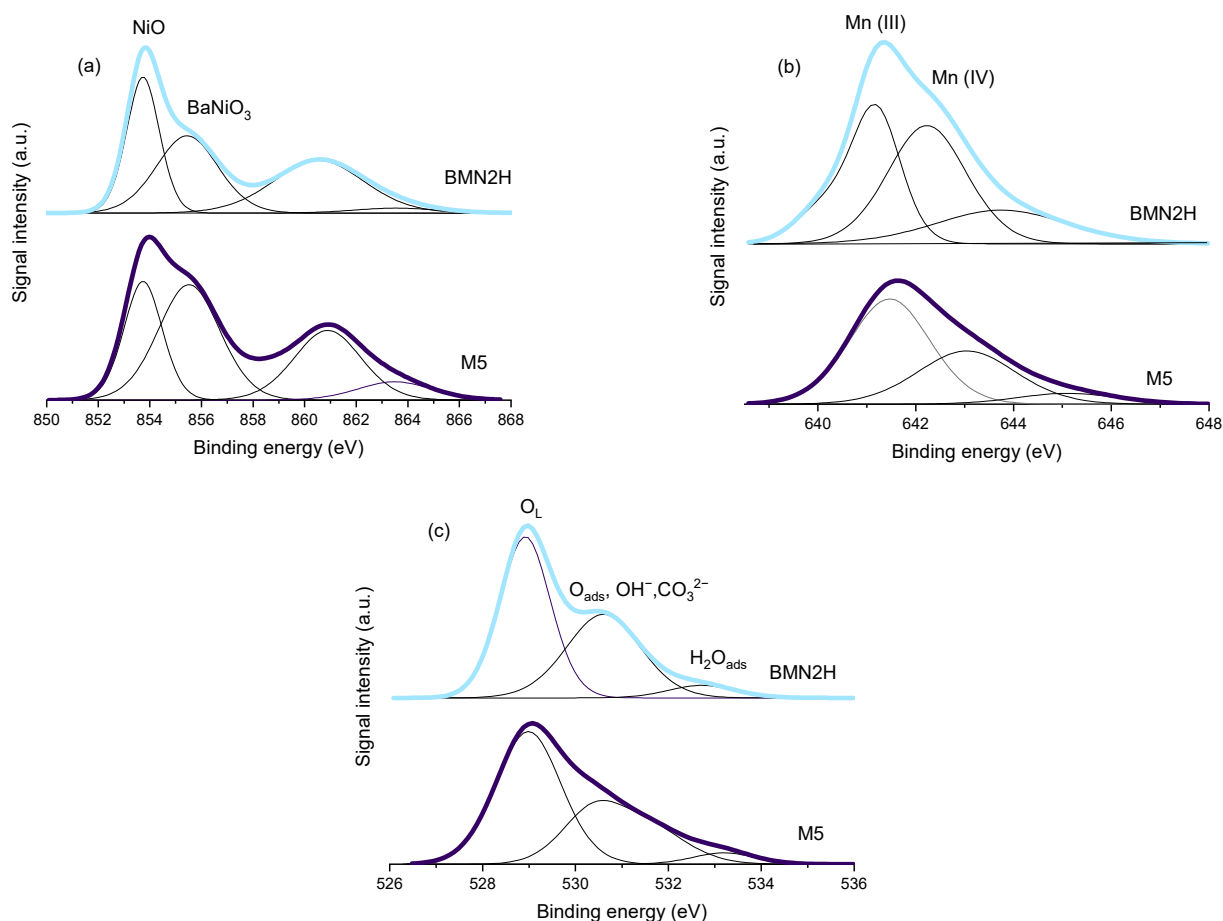

Figure 7. XPS spectra of the (**a**) Ni 2p$^{3/2}$, (**b**) Mn 2p$^{3/2}$, and (**c**) O1s transitions for M5 and BMN2H samples.

In Table 6, the $O_L/(Ba_L+Mn+Ni)$ ratio, estimated from the atomic percentages calculated by XPS and the area under the O_L deconvoluted peak, has been also included. Contrary to what might be expected, the BMN2H catalyst presents an $O_L/Mn+Ba_L+Ni$ ratio lower than the nominal one (1.5), revealing the presence of surface oxygen vacancies. However, for M5, the $O_L/Mn+Ba_L+Ni$ ratio is higher than the nominal one, so a higher proportion of lattice oxygen is present as the lattice oxygen corresponding to NiO is also included.

The reducibility of the samples was determined by a Temperature-Programmed Reduction with H_2 (H_2–TPR) and the profiles shown in Figure 8 present several reduction peaks between 200 °C and 1000 °C, corresponding to the reduction of Ni and Mn.

As mentioned above for BMN2E and BMN4E (Figure 3), three reduction peaks are detected [19,21,38]: (i) the first peak corresponds to the reduction of Mn(IV) and Mn(III) to Mn(II), and to the reduction of nickel, as the temperature for the manganese reduction is lower than for the BME sample [23,25]; (ii) the peak at intermediate temperatures, from 700 °C to 800 °C, is due to the reduction of surface oxygen species, and finally, (iii) the peak at high temperatures is assigned to the reduction of Mn(II) to Mn(0). For M5, the first peak appears at lower temperatures than for the BME support due not only to a pronounced synergistic Ni–Mn effect [25,40] but also because this sample presents a higher proportion

of NiO (see XPS and XRD results) which is reduced at lower temperatures [39]. The BMN2H sample presents two better defined reduction peaks, suggesting a less pronounced synergistic Mn-Ni effect than M5. Additionally, as the signal intensity is not completely decreased between the two peaks, the existence of a third overlapping peak is suggested. Thus, the reducibility of samples is in accordance with the higher reducibility of nickel from NiO than from $BaNiO_3$.
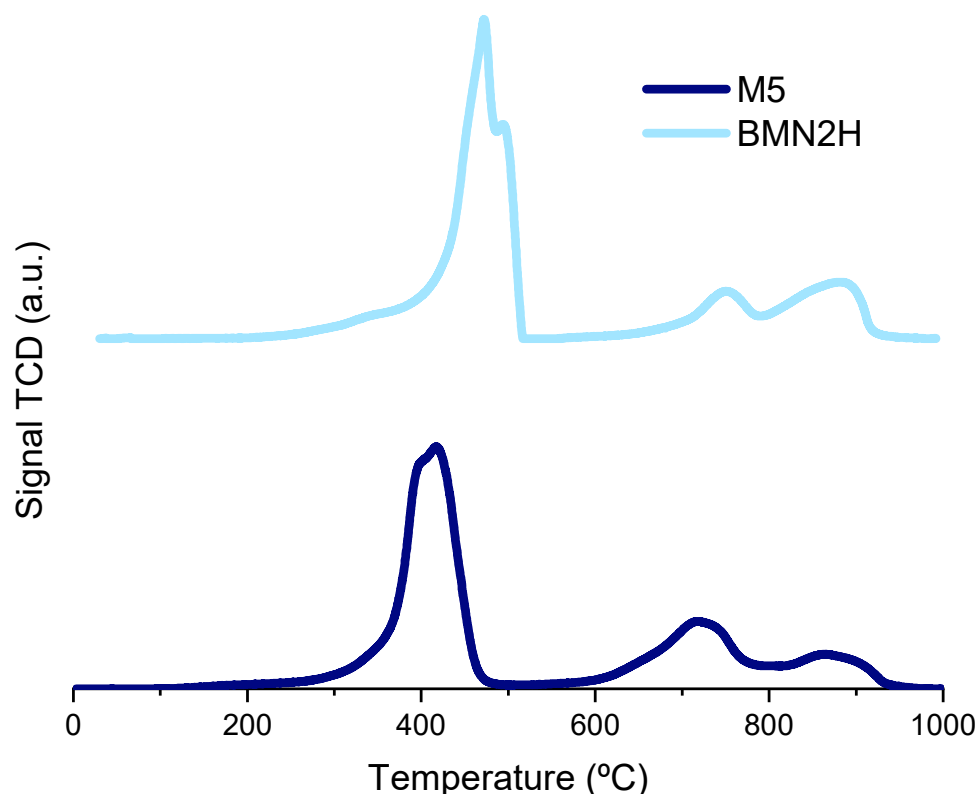
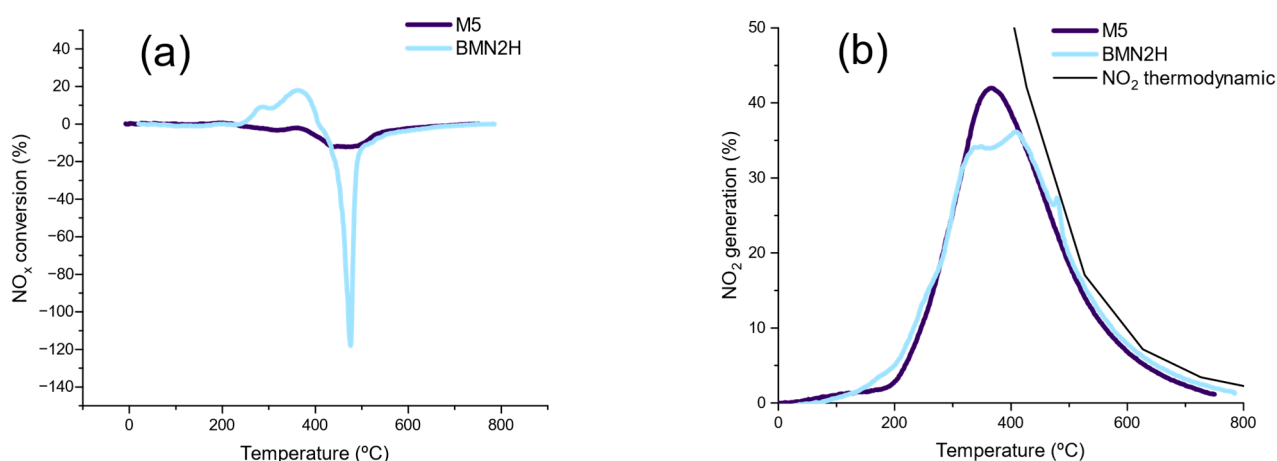**Figure 8.** H_2–TPR profiles for M5 and BMN2H samples.

2.2.2. Catalytic Activity Tests
NO to NO_2 Oxidation (NO_x–TPR)

Observing the NO_x conversion profiles shown in Figure 9a, it seems that M5 presents the lowest adsorption–desorption capacity, with BMN2H showing the highest one. Note that BMN2H features two maxima for the adsorption of NO_x and a pronounced desorption peak much higher than the one corresponding to NO_x adsorption (due to the NO_x being retained at room temperature before starting the test, which is not registered) [19–23]. So, it seems that the BMN2H catalyst should present much more active sites for NO_x adsorption at room temperature. This result agrees with the presence of $BaCO_3$ on BMN2H, which could also participate in the NO_x adsorption. Note that this sample presents a lower NiO average crystal size, so it has to present more nickel active sites.

Figure 9b presents the NO_2 generation profiles during NO_x–TPR experiments. The samples are active for the oxidation of NO to NO_2 at temperatures below 400 °C, with M5 evolving almost 40% of NO_2 at ca 400 °C and BMN2H showing two maxima: one of 35% at approximately 300 °C and another one of 37% at 435 °C; so, it seems that this sample has two active sites able to oxide NO to NO_2.

Figure 10a shows the Soot–NO_x–TPR profiles for the two nickel samples under comparison. At temperatures below 600 °C [21,22], both samples present higher soot conversion percentages than the observed uncatalyzed reaction (blank in Figure 10a). This trend is related to that observed for the NO_2 generation (Figure 9b) [19–23] as M5 and BMN2H present a better performance for soot oxidation and evolve a larger amount of NO_2.

Figure 9. (**a**) NO_X conversion profiles and (**b**) NO_2 generation profiles obtained under TPR conditions for M5 and BMN2H samples.
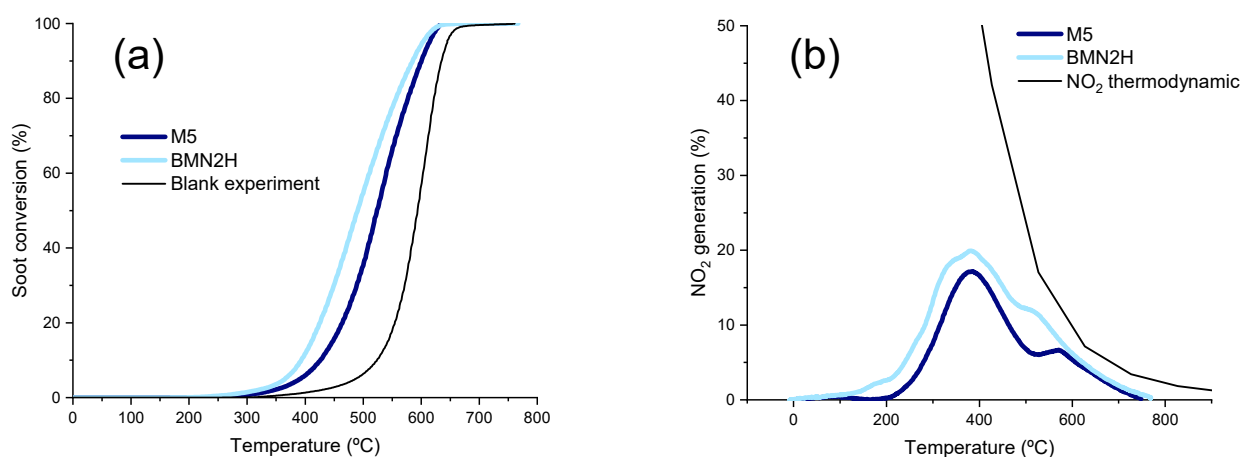

Figure 10. (**a**) Soot conversion and (**b**) NO_2 generation profiles in TPR conditions for M5 and BMN2H samples.

On the other hand, by comparing the NO_2 emission profiles in the absence and in the presence of soot (Figure 9b and Figure 10b, respectively), it seems that most of the NO_2 is being used for soot oxidation. To support this hypothesis, the NO_X conversion profiles in the absence (Figure 9a) and in the presence of soot (Figure 11) have been compared. The intensity of the desorption peak at 375 °C in the presence of soot for BMN2H is much lower than in the absence of soot as this sample is using a fraction of the NO_2 previously adsorbed for t soot oxidation. According to the XPS results, BMN2H presents more surface oxygen vacancies (Table 5) as the oxygen-deficient perovskite structure $BaNiO_{2.55}$ has been identified (Figure 6). The surface oxygen vacancies are active sites for oxidation reactions and improve the redox properties of the catalyst [42,43]. Additionally, BMN2H (due to the synthesis method used [44]) features a lower average crystal size that allows the presence of more nickel active sites on the surface (Table 5). Finally, as M5 accumulates more nickel on the surface, a lower amount of surface active sites should be present.

From the soot–TPR profiles shown in Figure 10, the temperature to achieve 50% soot conversion ($T_{50\%}$) was obtained and included in Table 7, where the selectivity to CO_2 (calculated by Equation (4)) is also featured. As expected, based on the soot–TPR profiles, both catalysts show a lower $T_{50\%}$ value and a higher selectivity to CO_2 than the uncatalyzed reaction (blank) and than BMN2E (see data in Table 4), with BMN2H presenting the lowest $T_{50\%}$ and the highest CO_2 selectivity, as expected since it has more surface active sites that favor the total soot oxidation [21–23,41]. This is because BMN2H presents a lower NiO

average crystal size than M5 (see XRD results, Table 5), so there is a higher number of active sites for soot oxidation. In addition, according to the XPS data (Table 6), BMN2H also shows a lower binding energy for Mn(III) and Mn(IV) than M5, which should also improve the redox properties.
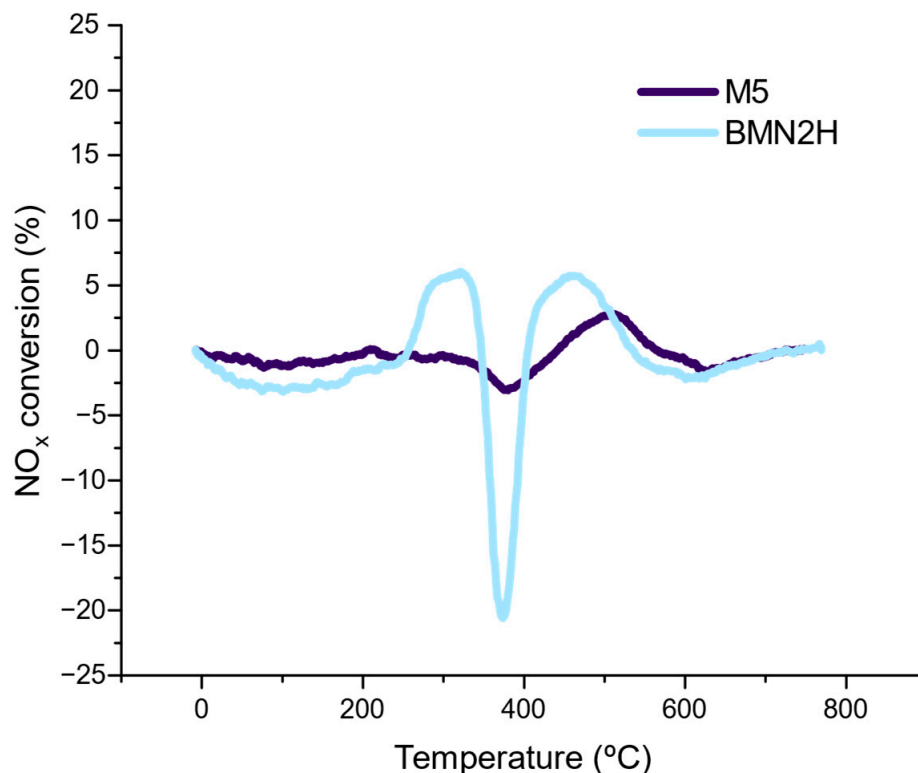
Figure 11. NO_X conversion profiles for M5 and BMN2H samples.

**Table 7.** $T_{50\%}$ and selectivity to CO_2 for M5 and BMN2H catalysts.

Sample	$T_{50\%}$ (°C)	Selectivity CO_2 (%)
M5	523 ± 8	92
BMN2H	490 ± 8	93
Blank	593 ± 8	38

Stability Tests

As BMN2H shows the best performance during the soot oxidation reaction in TPR conditions, the performance of this catalyst has been compared with one of the best catalysts found in our previous study, which is a nickel-iron barium perovskite ($BaFe_{0.6}Ni_{0.4}O_3$, denoted as BFN4E) [23,45,46].

From the soot conversion profiles at 450 °C, featured in Figure 12a, the soot oxidation rate for the BMN2H sample has been calculated, 56 μmol/min, which is more than two times the soot oxidation rate estimated for the BFN4E catalyst (25 μmol/min) [23]. So, BMN2H is more active to catalyze the NO_x-assisted soot oxidation reaction as it should present more nickel active sites than BFN4E [23].

Finally, to more deeply analyze the performance of the BMN2H catalyst, three consecutive soot reaction cycles at 450 °C were developed, with the soot conversion profiles shown in Figure 12b. The almost identical soot conversion profiles obtained should be a consequence of the high soot oxidation rate, which avoids the accumulation of soot during the reaction and, consequently, the deactivation of the catalyst.
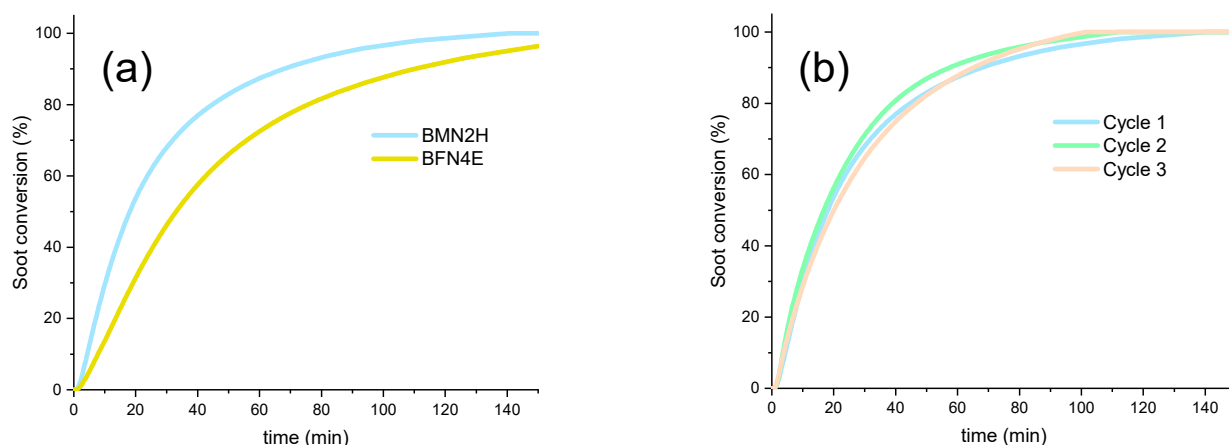
Figure 12. (**a**) Soot conversion profiles at 450 °C for BMN2H and BFN4E samples, and (**b**) soot conversion profiles in consecutive reaction cycles at 450 °C for BMN2H sample.

3. Experimental Section

3.1. Synthesis and Characterization of Catalysts

The $BaMn_{1-x}Ni_xO_3$ (x = 0, 0.2 and 0.4) samples were obtained by the sol–gel method [19–23,25,36,41,45,46] using citric acid and EDTA as complexing agents. Briefly, 40 mL of a solution of EDTA (Sigma–Aldrich, 98.5% purity) at 60 °C (in a 1:2 Mn: EDTA molar ratio) was prepared, followed by the addition of barium nitrate (Ba(NO$_3$)$_2$, Sigma–Aldrich, 99.0% purity), manganese(II) nitrate tetrahydrate (Mn(NO$_3$)$_2$·4 H$_2$O, Sigma–Aldrich, 99.0% purity), and nickel(II) nitrate hexahydrate (Ni(NO$_3$)$_2$·6 H$_2$O, Panreac, 98.0% purity) as metal precursors, and finally, citric acid (C$_6$H$_8$O$_7$, Sigma–Aldrich, 99.0% purity) was incorporated in the same molar ratio than of EDTA (1:2, Mn: citric acid). Subsequently, using an ammonia solution (Panreac, 30 wt %), the pH of the solution was increased until it reached 9. This solution was kept at 80 °C (5 h) to ensure gel formation and the obtained gel was dried at 150 °C for 12 h. Finally, the solid was calcined at 850 °C for 6 h.

Additionally, a 5 wt % Ni/BaMnO$_3$ sample was prepared by the incipient wetness impregnation method [47,48]. First, the BaMnO$_3$ perovskite to be employed as a support was synthesized using the sol–gel method previously described for the $BaMn_{1-x}Ni_xO_3$ samples. After, the support was impregnated with the volume of a Ni(NO$_3$)$_2$·6 H$_2$O solution (containing the desired amount of nickel) needed to wet the solid. Then, it was stirred at room temperature for 24 h, dried at 90 °C for 24 h and, finally, calcined at 500 °C for 12 h. BaMn$_{0.8}$Ni$_{0.2}$O$_3$ was also synthesized by a hydrothermal method [44,45], using barium hydroxide octahydrate (Ba(OH)$_2$ *8 H$_2$O, Sigma–Aldrich, 98.0% purity), a potassium permanganate and manganese(IV) oxide mixture (KMnO$_4$, Sigma-Aldrich, 99.0% purity; MnO$_2$, Sigma–Aldrich, St. Louis, MO, USA, 99.0% purity) (1:3, respectively), and Ni(NO$_3$)$_2$·6 H$_2$O as precursors. For the synthesis, Ba(OH)$_2$ *8 H$_2$O was dissolved in 25 mL of water and heated to 90 °C (without stirring) for 1 h. Later, manganese and nickel precursors were added under stirring at room temperature for 15 min and, subsequently, the solution was basified with potassium hydroxide (KOH, Sigma–Aldrich, 85.0% purity) until saturation. Then, the resulting solution was treated at 90 °C in an autoclave for 72 h. The obtained solid was filtered, washed, and dried at 90 °C overnight. Finally, a calcination step (600 °C for 6 h) was carried out.

For sample characterization, several techniques were used.

The nickel content was determined by ICP–OES on a Perkin–Elmer device model Optimal 4300 DV. For the analysis, the elements were extracted from the samples with a diluted aqua regia solution (by stirring at 60 °C for 1 h).

The textural properties were estimated by N$_2$ adsorption at −196 °C using an Autosorb–6B instrument from Quantachrome (Anton Paar Austria GmbH, Graz, Austria). Before the N$_2$ adsorption experiments, the samples were degassed at 250 °C (4 h).

X-Ray Diffraction (XRD) was used to obtain information about the crystalline structure, with the X-ray patterns recorded between 20 and 80° 2θ angles (with a step rate of 0.4°/min and using Cu K_α (0.15418 nm) radiation) in a Bruker D8-Advance device.

X-Ray Photoelectron Spectroscopy (XPS) was employed for surface chemistry characterization. A K–Alpha Photoelectron Spectrometer by Thermo–Scientific with an Al K_α (1486.7 eV) radiation source was used, and to obtain the XPS spectra, the pressure of the analysis chamber was maintained at 5×10^{-10} mbar. The binding energy (BE) and kinetic energy (KE) scales were adjusted by setting the C 1s transition at 284.6 eV, and the BE and KE values were then determined with the peak-fit software of the spectrometer. The $O_L/(Ba+Mn+Ni)$, $Ni/(Ba+Mn+Ni)$, and $Mn(IV)/Mn(III)$ XPS ratios were calculated using the area under the suggested deconvoluted bands of O 1s, Ba $3d^{5/2}$, Mn $2p^{3/2}$, and Ni $2p^{3/2}$ transitions.

The reducibility of the samples was estimated by a Temperature-Programmed Reduction with H_2 (H_2–TPR) in a Pulse Chemisorb 2705 (from Micromeritics) fitted with a Thermal Conductivity Detector (TCD). Then, 30 mg of the sample was heated at 10 °C/min from 25 to 1000 °C in a 5% H_2/Ar atmosphere (40 mL/min); for the H_2 consumption quantification, a CuO reference sample was used.

3.2. Activity Tests

To determine the activity for NO to NO_2 oxidation and NO_x-assisted diesel soot oxidation, a Temperature-Programmed Reaction was carried out. A quartz fixed-bed reactor, heated up from 25 to 800 °C (10 °C/min) under a gas flow mixture (500 mL/min) containing 500 ppm NO_X and 5% O_2 balanced with N_2 was employed. For the NO to NO_2 experiments (NO_X–TPR), 80 mg of catalyst was diluted with 320 mg of SiC, and for soot oxidation tests (Soot-NO_X–TPR), 80 mg of catalyst and 20 mg of Printex–U (the carbon black used as model soot) were mixed with a spatula to ensure loose contact; after, the mixture was diluted with 300 mg of SiC. The most active catalyst was also tested under isothermal soot oxidation conditions at 450 °C for 3 h and for testing the recyclability of the catalyst, three isothermal cycles at 450 °C were performed. The gas composition was determined by using specific NDIR–UV gas analyzers (for NO, NO_2, CO, CO_2, and O_2 from Rosemount Analytical Model BINOS 1001, 1004, and 100, Emerson Electric Co., St. Louis, MO, USA). The NO_x conversion and the NO_2 generation percentages were calculated using the following equations:

$$NO_x \text{ conversion}(\%) = \frac{(NO_{x,in} - NO_{x,out})}{NO_{x,in}} \cdot 100 \tag{1}$$

$$NO_{2,out}/NO_{x,out}(\%) = \frac{NO_{2,out}}{NO_{x,out}} \cdot 100 \tag{2}$$

where $NO_{2,out}$ and $NO_{X,out}$ are the NO_2 and NO_x (NO + NO_2) concentrations measured at the reactor exit (i.e., after reaction) and $NO_{X,in}$ is the NO + NO_2 concentrations measured at the reactor inlet (i.e., before reaction).

The percentage of soot conversion and the CO_2 selectivity were determined as follows:

$$\text{Soot conversion}(\%) = \frac{\sum_0^t CO_2 + CO}{\sum_0^{final} (CO_2 + CO)} \cdot 100 \tag{3}$$

$$CO_2 \text{ Selectivity}(\%) = \frac{CO_2}{\sum_0^{final} (CO_2 + CO)} \cdot 100 \tag{4}$$

where $\sum_0^t (CO_2 + CO)$ is the amount of CO_2 and CO evolved at a time t, while $\sum_0^{final} CO_2$ and $\sum_0^{final} (CO_2 + CO)$ are the total amount of CO_2 and CO + CO_2 evolved during the test.

4. Conclusions

In this work, $BaMn_{1-x}Ni_xO_3$ (x = 0, 0.2, and 0.4) samples were prepared to estimate the effect of the nickel amount on the partial substitution of Mn by Ni. These catalysts have been characterized and tested for the oxidation of NO to NO_2 and for the NO_x-assisted diesel soot oxidation. Additionally, for the selected nickel content (5 wt %), the effect of the nickel addition method on the catalytic performance was analyzed by using the hydrothermal method (BMN2H) and the incipient wetness impregnation method (M5). From the discussion of characterization and activity results, the following conclusions can be obtained:

- Nickel is not incorporated into the lattice of the $BaMnO_3$ perovskite as it forms a $BaNiO_3$ perovskite. If the sol–gel or hydrothermal method is used for nickel addition, an oxygen-deficient perovskite structure ($BaNiO_{2.55}$) is also detected.
- Mn(III) and Mn(IV) oxidation states coexist on the surface of samples, with Mn(IV) being the main one in most of them. $BaMn_{1-x}Ni_xO_3$ catalysts present oxygen vacancies to compensate for the positive charge imbalance caused by the presence of Mn(III) and Ni(II).
- For nickel samples, a Ni–Mn synergistic effect exists which decreases the manganese reduction temperature during H_2–TPR.
- All samples increase the activity for the oxidation of NO and soot at T < 400 °C, with the nickel-containing samples showing the highest activity. BMN2E and BMN4E also present a higher selectivity to CO_2 than BME, so it seems that nickel catalysts have more active sites for total soot oxidation. However, no effect of nickel amount in the catalytic performance was observed.
- The method used for nickel addition to $BaMnO_3$ perovskite seems to be relevant as BMN2H, synthetized by hydrothermal procedure, is more active than M5 (obtained by incipient wetness impregnation of $BaMnO_3$) and than BMN2E (obtained by the sol–gel method) as it presents: (i) more surface oxygen vacancies which are active sites for oxidation reactions, (ii) improved redox properties, and (iii) a lower NiO average crystal size which enables a higher amount of nickel active sites for NO and soot oxidation. As a consequence of these properties, BMN2H features a high soot oxidation rate, which minimizes the accumulation of soot and, thus, the deactivation of the catalyst during the reaction.

Data Availability Statement: Data are contained within the article.

Conflicts of Interest: The authors declare no conflict of interest.

References

1. Cunanan, C.; Tran, M.-K.; Lee, Y.; Kwok, S.; Leung, V.; Fowler, M.A. Review of Heavy-Duty Vehicle Powertrain Technologies: Diesel Engine Vehicles, Battery Electric Vehicles, and Hydrogen Fuel Cell Electric Vehicles. *Clean. Technol.* **2021**, *3*, 474–489. [CrossRef]
2. Ahmadi, P.; Khoshnevisan, A. Dynamic simulation and lifecycle assessment of hydrogen fuel cell electric vehicles considering various hydrogen production methods. *Int. J. Hydrogen Energy* **2022**, *47*, 26758–26769. [CrossRef]
3. Joyn, N.; Balan, K.N.; Nagappan, B.; Abraham-baby, S.J. Emission analysis of diesel and butanol blends in research diesel engine. *Pet. Sci. Technol.* **2020**, *38*, 289–296. [CrossRef]

4. Leach, F.; Kalghatgi, G.; Stone, R.; Miles, P. The scope for improving the efficiency and environmental impact of internal combustion engines. *Trans. Eng.* **2020**, *1*, 100005. [CrossRef]

5. Ayodhya, A.S.; Narayanappa, K.G. An overview of after-treatment systems for diesel engines. *Environ. Sci. Pollut. Res.* **2018**, *25*, 35034–35047. [CrossRef] [PubMed]

6. Yu, T.; Li, K.; Wu, Q.; Yao, P.; Ke, J.; Wang, B.; Wang, Y. Diesel Engine Emission Aftertreatment Device Aging Mechanism and Durability Assessment Methods: A Review. *Atmosphere* **2023**, *14*, 314. [CrossRef]

7. Legutko, P.; Stelmachowski, P.; Yu, X.; Zhao, Z.; Sojka, Z.; Kotarba, A. Catalytic Soot Combustion-General Concepts and Alkali Promotion. *ACS Catal.* **2023**, *13*, 3395–3418. [CrossRef]

8. Dey, S.; Mehta, N.S. Automobile pollution control using catalysis. *Resour. Environ. Sustain.* **2020**, *2*, 100006. [CrossRef]

9. Sanchez, A. *The Contribution of Transport to Air Quality TERM 2012: Transport Indicators Tracking Progress towards Environmental Targets in Europe*; European Environment Agency: Copenhagen, Denmark, 2012.

10. DieselNet. Available online: https://www.dieselnet.com (accessed on 24 September 2023).

11. Jung, Y.; Pyo, Y.D.; Jang, J.; Kim, G.C.; Cho, C.P.; Yang, C. NO, NO_2 and N_2O emissions over a SCR using DOC and DPF systems with Pt reduction. *Chem. Eng. J.* **2019**, *369*, 1059–1067. [CrossRef]

12. Lee, J.H.; Jo, D.Y.; Choung, J.W.; Kim, C.H.; Ham, H.C.; Lee, K.Y. Roles of noble metals (M = Ag, Au, Pd, Pt and Rh) on CeO_2 in enhancing activity toward soot oxidation: Active oxygen species and DFT calculations. *J. Hazard. Mater.* **2021**, *403*, 124085. [CrossRef]

13. Zhang, Z.; Dong, R.; Lan, G.; Yuan, T.; Tan, D. Diesel particulate filter regeneration mechanism of modern automobile engines and methods of reducing PM emissions: A review. *Environ. Sci. Pollut. Res.* **2023**, *30*, 39338–39376. [CrossRef] [PubMed]

14. Garba, Z.N.; Zhou, W.; Zhang, M.; Yuan, Z. A Review on the Preparation, Characterization and Potential Application of Perovskites as Adsorbents for Wastewater Treatment. *Chemosphere* **2020**, *244*, 125474. [CrossRef] [PubMed]

15. Zhu, J.; Li, H.; Zhong, L.; Xiao, P.; Xu, X.; Yang, X.; Zhao, Z.; Li, J. Perovskite Oxides: Preparation, Characterizations, and Applications in Heterogeneous Catalysis. *ACS Catal.* **2014**, *4*, 2917–2940. [CrossRef]

16. Jiang, Y.; Li, Z.; Zhu, T.; Li, D.; Wang, H.; Zhu, X. Oxygen Storage Characteristics and Redox Behaviors of Lanthanum Perovskite Oxides with Transition Metals in the B-Sites. *Energy Fuels* **2023**, *37*, 9419–9433. [CrossRef]

17. Wu, X.; Fischer, M.; Nolte, A.; Lenßen, P.; Wang, B.; Ohlerth, T.; Wöll, D.; Heufer, K.A.; Pischinger, S.; Simon, U. Perovskite Catalyst for In-Cylinder Coating to Reduce Raw Pollutant Emissions of Internal Combustion Engines. *ACS Omega* **2022**, *7*, 5340–5349. [CrossRef]

18. Onrubia-Calvo, J.A.; Pereda-Ayo, B.; Urrutxua, M.; De La Torre, U.; González-Velasco, J.R. Boosting NO_x Removal by Perovskite-Based Catalyst in NSR–SCR Diesel Aftertreatment Systems. *Ind. Eng. Chem. Res.* **2021**, *60*, 6525–6537. [CrossRef]

19. Díaz Verde, A.; Montilla Verdú, S.; Torregrosa Rivero, V.; Illán Gómez, M.J. Tailoring the Composition of Ba_xBO_3 (B = Fe, Mn) Mixed Oxides as CO or Soot Oxidation Catalysts in Simulated GDI Engine Exhaust Conditions. *Molecules* **2023**, *28*, 3327. [CrossRef]

20. Torregrosa Rivero, V.; Sánchez-Adsuar, M.S.; Illán Gómez, M.J. $BaFe_{1-x}Cu_xO_3$ Perovskites as Active Phase for Diesel (DPF) and Gasoline Particle Filters (GPF). *Nanomaterials* **2019**, *9*, 1551. [CrossRef]

21. Torregrosa Rivero, V.; Sánchez-Adsuar, M.S.; Illán Gómez, M.J. Analyzing the role of copper in the soot oxidation performance of $BaMnO_3$-perovskite-based catalyst obtained by modified sol-gel synthesis. *Fuel* **2022**, *328*, 125258. [CrossRef]

22. Torregrosa Rivero, V.; Sánchez-Adsuar, M.S.; Illán Gómez, M.J. Improving the Performance of $BaMnO_3$ Perovskite as Soot Oxidation Catalyst Using Carbon Black during Sol-Gel Synthesis. *Nanomaterials* **2022**, *12*, 219. [CrossRef]

23. Montilla Verdú, S.; Torregrosa Rivero, V.; Díaz Verde, A.; Illán Gómez, M.J. $BaFe_{1-x}Ni_xO_3$ Catalysts for NOx-Assisted Diesel Soot Oxidation. *Top. Catal.* **2023**, *66*, 839–849. [CrossRef]

24. Royer, S.; Duprez, D.; Can, F.; Courtois, X.; Batiot-Dupeyrat, C.; Laassiri, S.; Alamdari, H. Perovskites as Substitutes of Noble Metals for Heterogeneous Catalysis: Dream or Reality. *Chem. Rev.* **2014**, *114*, 10292–10368. [CrossRef] [PubMed]

25. Torregrosa Rivero, V.; Sánchez-Adsuar, M.S.; Illán Gómez, M.J. Exploring the effect of using carbon black in the sol-gel synthesis of $BaMnO_3$ and $BaMn_{0.7}Cu_{0.3}O_3$ perovskite catalysts for CO oxidation. *Catal. Today* **2023**, *423*, 114028. [CrossRef]

26. Atkins, P.W.; Overton, T.; Rourke, J.; Weller, M.; Armstrong, F.; Hagerman, M. *Shriver & Atkins' Inorganic Chemistry*, 5th ed.; W.H. Freeman and Company, Ed.; Oxford University Press: Oxford, UK, 2010.

27. Venezia, A.M. X-ray photoelectron spectroscopy (XPS) for catalysts characterization. *Catal. Today* **2003**, *77*, 359–370. [CrossRef]

28. Ao, R.; Ma, L.; Dai, Q.; Guo, Z.; Liu, H.; Xiong, X.; Pan, Q. Simultaneous catalytic oxidation of NO and Hg^0 over $LaBO_3$ (B = Co, Mn, Ni, and Cu) perovskites. *J. Environ. Chem. Eng.* **2021**, *9*, 106612. [CrossRef]

29. Gottschall, R.; Schöllhorn, R.; Muhler, M.; Jansen, N.; Walcher, D.; Gütlich, P. Electronic state of nickel in barium nickel oxide, $BaNiO_3$. *Inorg. Chem.* **1998**, *37*, 1513–1518. [CrossRef]

30. Lee, J.G.; Hwang, H.J.; Kwon, O.; Jeon, O.K.; Jang, J.; Shul, Y.-G. Synthesis and application of hexagonal perovskite $BaNiO_3$ with quadrivalent nickel under atmospheric and low-temperature conditions. *Chem. Commun.* **2016**, *52*, 10731. [CrossRef]

31. Zhang, C.; Wang, C.; Hua, W.; Guo, Y.; Lu, G.; Gil, S.; Giroir-Fendler, A. Relationship between Catalytic Deactivation and Physicochemical Properties of $LaMnO_3$ Perovskite Catalyst during Catalytic Oxidation of Vinyl Chloride. *Appl. Catal. B Environ.* **2016**, *186*, 173–183. [CrossRef]

32. Cimino, S.; Lisi, L.; De Rossi, S.; Faticanti, M.; Porta, P. Methane combustion and CO oxidation on $LaAl_{1-x}Mn_xO_3$ perovskite-type oxide solid solutions. *Appl. Catal. B Environ.* **2003**, *43*, 397–406. [CrossRef]

33. Teraoka, Y.; Nii, H.; Kagawa, S.; Jansson, K.; Nygren, M. Influence of the simultaneous substitution of Cu and Ru in the perovskite-type (La,Sr)MO$_3$ (M = Al, Mn, Fe, Co) on the catalytic activity for CO oxidation and CO-NO reactions. *Appl. Catal. A Gen.* **2000**, *194–195*, 35–41. [CrossRef]

34. Petrolekas, P.D.; Metcalfe, I.S. Solid Electrolyte Potentiometric Study of La(Sr)MnO$_3$ Catalyst During Carbon-Monoxide Oxidation. *J. Catal.* **1995**, *152*, 147–163. [CrossRef]

35. Patcas, F.; Buciuman, F.C.; Zsako, J. Oxygen Non-Stoichiometry and Reducibility of B-Site Substituted Lanthanum Manganites. *Thermochim. Acta* **2000**, *360*, 71–76. [CrossRef]

36. Moreno Marcos, C.; Torregrosa Rivero, V.; Albaladejo Fuentes, V.; Sánchez-Adsuar, M.S.; Illán Gómez, M.J. BaFe$_{1-x}$Cu$_x$O$_3$ Perovskites as Soot Oxidation Catalysts for Gasoline Particulate Filters (GPF): A Preliminary Study. *Top. Catal.* **2019**, *62*, 413–418. [CrossRef]

37. Merino, N.A.; Barbero, B.P.; Eloy, P.; Cadús, L.E. La$_{1-x}$Ca$_x$CoO$_3$ perovskite-type oxides: Identification of the surface oxygen species by XPS. *Appl. Surf. Sci.* **2006**, *253*, 1489–1493. [CrossRef]

38. Liu, L.; Sun, J.; Ding, J.; Zhang, Y.; Jia, J.; Sun, T. Catalytic oxidation of VOCs over SmMnO$_3$ perovskites: Catalyst synthesis, change mechanism of active species, and degradation path of toluene. *Inorg. Chem.* **2019**, *58*, 14275–14283. [CrossRef]

39. Bai, C.-S.; Soled, S.; Kershaw, R.; Dwight, K.; Wold, A. The Preparation and Characterization of the Phases Formed by the Reactions of Nickel and Lanthanum Nitrates with Magnesium Aluminate. *J. Solid State Chem.* **1992**, *100*, 307–312. [CrossRef]

40. Torregrosa-Rivero, V.; Albaladejo-Fuentes, V.; Sánchez-Adsuar, M.S.; Illán-Gómez, M.J. Copper Doped BaMnO$_3$ Perovskite Catalysts for NO Oxidation and NO$_2$-Assisted Diesel Soot Removal. *RSC Adv.* **2017**, *7*, 35228–35238. [CrossRef]

41. Díaz-Verde, A.; Torregrosa-Rivero, V.; Illán-Gómez, M.J. Copper Catalysts Supported on Barium Deficient Perovskites for CO Oxidation Reaction. *Top. Catal.* **2023**, *66*, 895–907. [CrossRef]

42. Luo, Y.; Zheng, Y.; Feng, X.; Lin, D.; Qian, Q.; Wang, X.; Zhang, Y.; Chen, Q.; Zhang, X. Controllable P Doping of the LaCoO$_3$ Catalyst for Efficient Propane Oxidation: Optimized Surface Co Distribution and Enhanced Oxygen Vacancies. *ACS Appl. Mater. Interfaces* **2020**, *12*, 23789–23799. [CrossRef]

43. Yang, J.; Hu, S.; Fang, Y.; Hoang, S.; Li, L.; Yang, W.; Liang, Z.; Wu, J.; Hu, J.; Xiao, W.; et al. Oxygen Vacancy Promoted O$_2$ Activation over Perovskite Oxide for Low-Temperature CO Oxidation. *ACS Catal.* **2019**, *9*, 9751–9763. [CrossRef]

44. Pereñiguez, R.; Gonzalez de la Cruz, V.M.; Caballero, A.; Holgado, J.P. LaNiO$_3$ as a precursor of Ni/La$_2$O$_3$ for CO$_2$ reforming of CH$_4$: Effect of the presence of an amorphous NiO phase. *Appl. Catal. B Environ.* **2012**, *123–124*, 324–332. [CrossRef]

45. Torregrosa-Rivero, V.; Sánchez-Adsuar, M.S.; Illán-Gómez, M.J. Modified BaMnO$_3$-Based Catalysts for Gasoline Particle Filters (GPF): A Preliminary Study. *Catalysts* **2022**, *12*, 1325. [CrossRef]

46. Navas, D.; Fuentes, S.; Castro-Álvarez, A.; Chavez-Ángel, E. Review on Sol-Gel Synthesis of Perovskite and Oxide Nanomaterials. *Gels* **2021**, *7*, 275. [CrossRef] [PubMed]

47. Kumar Yadav, P.; Das, T. Production of syngas from carbon dioxide reforming of methane by using LaNi$_x$Fe$_{1-x}$O$_3$ perovskite type catalysts. *Int. J. Hydrogen Energy* **2019**, *44*, 1659–1670. [CrossRef]

48. Mortazavi-Manesh, A.; Safari, N.; Bahadoran, F.; Khani, Y. Synthesis, characterization, and methanol steam reforming performance of Cu/perovskite-structured catalysts. *Heliyon* **2023**, *9*, 13742. [CrossRef]